First-Principles Investigations of Metal (Cu, Ag, Au, Pt, Rh, Pd, Fe, Co, and Ir) Doped Hexagonal Boron Nitride Nanosheets: Stability and Catalysis of CO Oxidation

4 AUTHORS, INCLUDING:

Sen Lin
Fuzhou University
40 PUBLICATIONS **541** CITATIONS

SEE PROFILE

Ryan S Johnson
University of New Mexico
13 PUBLICATIONS **130** CITATIONS

SEE PROFILE

Hua Guo
University of New Mexico
**382** PUBLICATIONS **7,575** CITATIONS

SEE PROFILE

First-Principles Investigations of Metal (Cu, Ag, Au, Pt, Rh, Pd, Fe, Co, and Ir) Doped Hexagonal Boron Nitride Nanosheets: Stability and Catalysis of CO Oxidation

Sen Lin,*,[†] Xinxin Ye,[†] Ryan S. Johnson,[‡] and Hua Guo[‡]

[†]Research Institute of Photocatalysis, Fujian Provincial Key Laboratory of Photocatalysis, State Key Laboratory Breeding Base, Fuzhou University, Fuzhou 350002, China

[‡]Department of Chemistry and Chemical Biology, University of New Mexico, Albuquerque, New Mexico 87131, United States

ABSTRACT: By means of first-principles computation, metal (Cu, Ag, Au, Pt, Rh, Pd, Fe, Co, and Ir) doped hexagonal boron nitride nanosheets (h-BNNSs) have been systematically investigated. The strong interaction between the metal atoms and defect sites in h-BNNS, such as the boron vacancy and nitrogen edge, suggests that metal doped h-BN nanosheets (M-BNNSs) should be stable under high temperatures. The catalytic activity of Co doped h-BNNS is also investigated by using CO oxidation as a probe, and the calculated low barrier suggests that the Co-BNNS is a viable catalyst for CO oxidation. Based on electronic structure analysis, the catalytic capacity of Co-BNNS is attributed to the strong mixing between the cobalt 3d orbitals and oxygen 2p orbitals, which activates the adsorbed molecular or atomic oxygen.
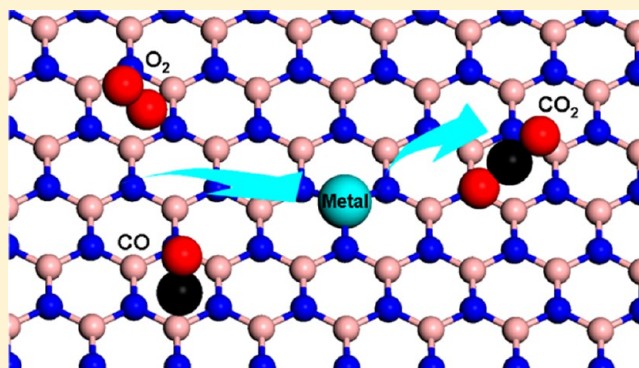
I. INTRODUCTION

Metal subnanoclusters supported on a graphene sheet have been found to exhibit an unusually high activity for oxidation reactions,[1] making them attractive candidates for next-generation catalysts. Furthermore, recent theoretical studies suggested that single metal atoms, such as Au, Cu, and Fe, embedded in graphene or graphene oxide possess a high catalytic activity for CO oxidation as well.[2−5] These studies suggest a possible new direction in designing future catalysts with high efficiency. Other graphene-like materials, e.g., hexagonal boron nitride (h-BN), have also attracted considerable attention due to their exceptional physical and chemical properties for various applications.[6−13] In particular, h-BNNS exhibits superb thermal stability, high thermal conductivity, and high electrical resistance. Although the defect-free h-BN is probably too stable to influence the physical and chemical properties of deposited metal atoms and clusters, h-BNNSs, particularly those with defects, share many characteristics with graphene and might provide a useful template for developing new catalysts via metal atom doping. Importantly, unlike graphene-based materials which are observed to burn at temperatures below 800 K, h-BNNSs remain stable at much higher temperatures, up to 1000 K.[14,15]

Some lattice defects in h-BNNSs, such as boron and nitrogen vacancies, have been identified by Jin et al.[16] via direct imaging after controlled energetic electron beam irradiation. These observations were investigated theoretically by Du and co-workers, in which a boron monovacancy was found to have a lower formation energy than the nitrogen monovacancy.[17]

Thanks to these defect sites, the h-BNNS can be transformed from an inert material to a potentially active catalyst through embedding its defect sites with metal atoms.[18−20] The resulting M-BNNS might exhibit different catalytic properties from the bulk metals due to their different unsaturated metal sites.

Using a plane-wave density functional theory (DFT) method, we have recently suggested that h-BNNSs are capable of accepting ruthenium atoms at their defect sites, and the resulting Ru-BNNS has a low energy barrier for CO oxidation.[21] The single metal atom catalysis differs significantly from that of the bulk Ru metal, which has a much higher reaction barrier.[22] Despite this initial work, our knowledge of the stability and catalytic activity of M-BNNS is still quite primitive, due to the lack of a comprehensive understanding of the interaction between various metal atoms and the h-BNNSs. Three primary questions about the nature of the M-BNNS remain to be settled: (1) How do various metals atoms interact with the defect sites of h-BNNSs? (2) Can M-BNNSs remain stable at high temperatures? (3) Can M-BNNSs have high catalytic activity for reactions such as CO oxidation?

In this work, we present an extensive theoretical investigation of the geometries and stability of several other M-BNNSs (M = Cu, Ag, Au, Pt, Rh, Pd, Fe, Co, and Ir, which are usually adopted as the catalysts for CO oxidation[23]) by using the same plane-wave DFT method as in our earlier work.[21] In order to
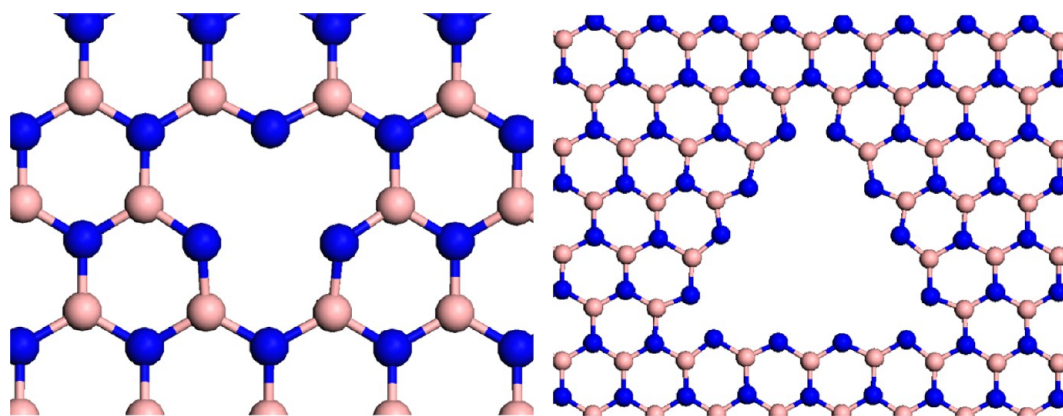
Figure 1. Geometries (top view) of h-BNNS with the B-vacancy (left) and N-edge (right) defects. Color scheme: B, pink; N, dark blue.

Table 1. Geometrical Parameters (Å) for the Metal-Embedded h-BNNS with the B-Vacancy, Bader Charge and Binding Energy (eV) for Metal Atom at the B-Vacancy, and Binding Energies (eV) for CO and O$_2$ at the Metal Site

metal (M)	M-sheet distance	M−N distance	Bader charge ($|e|$)	E_b (M)	E_b (CO)	E_b (O$_2$)	O−O distance
Cu	1.14	1.83	0.89	−5.64	−0.84	−0.54	1.33
Fe	1.08	1.77	1.02	−8.54	−1.35	−2.34	1.39
Ag	1.66	2.12	0.69	−3.02	−1.07	−0.84	1.31
Co	1.03	1.75	0.90	−8.64	−1.15	−1.41	1.36
Au	1.58	2.07	0.64	−3.03	−1.70	−1.37	1.34
Pt	1.42	1.97	0.68	−6.53	−2.03	−2.01	1.35
Ir	1.34	1.91	0.80	−9.21	−2.29	−2.37	1.43
Rh	1.34	1.91	0.77	−8.41	−1.54	−1.42	1.38
Pd	1.42	1.97	0.70	−5.24	−1.27	−1.50	1.32

better understand the catalytic activity of M-BNNSs, CO oxidation was chosen as a benchmark probe reaction. Both kinetic and thermodynamic information were obtained for this prototypical reaction on a Co doped h-BNNS. This publication is organized as follows. The calculation details are described in section 2. The results and discussion are presented in section 3. Finally, the conclusions are given in section 4.

2. CALCULATION DETAILS

The plane-wave density functional theory (DFT) calculations were carried out by using the Vienna *ab initio* simulation package (VASP)[24−26] with the gradient-corrected PW91 exchange-correction functional.[27] For valence electrons, a plane-wave basis set was adopted with an energy cutoff of 400 eV and the ionic cores were described with the projector augmented-wave (PAW) method.[28,29] The optimized lattice parameter for a h-BN monolayer was calculated to be 2.50 Å, which is in excellent agreement with the previously reported experimental[30] and theoretical results.[17,21,31] This infinitely spanned h-BN monolayer provides an approximated model for h-BNNSs.

Two types of defects are studied in this work: one is a simple point defect boron vacancy (denoted as B-vacancy), and the other is the nitrogen atom exposed edge (denoted as N-edge) as observed in the triangular nanoholes of h-BNNSs[16] and are displayed in Figure 1. A 3 × 3 × 1 unit cell for a monolayer h-BNNS with a B-vacancy was constructed as a substrate and a single metal atom (Cu, Ag, Au, Pt, Rh, Pd, Fe, Co, or Ir) was embedded in the B-vacancy. On the other hand, an 8 × 8 × 1 unit cell for a monolayer h-BNNS with a trigonal vacancy with the N-edge was also constructed, and a single Co atom was embedded at the N-edge. 2 × 2 × 1 and 1 × 1 × 1 Monkhorst−

Pack k-point grids were used to sample the Brillouin zone[32] of h-BN monolayers with the B-vacancy and N-edge, respectively, which were tested to be converged. All the atoms in the unit cell including adsorbates were allowed to relax during the optimization. Spin polarization was adopted in all calculations of metal doped defect h-BNNSs. In order to avoid the interlayer interactions, a vacuum spacing was set to be 14 Å. For the calculation of the local density of states (LDOS), an 11 × 11 × 1 Monkhorst−Pack k-point grid for h-BNNS with the B-vacancy and a 7 × 7 × 1 for h-BNNS with the N-edge were employed, respectively, which were tested to be sufficient to yield accurate results.

The binding energy was defined as E_b = E(adsorbate + sheet) − E(free molecule or atom) − E(free sheet). The nudged elastic band (NEB) method[33] was used to locate transition states, and the minimum energy path (MEP) was constructed accordingly. In order to ensure accuracy, at least 12 images were used in each NEB calculation. The highest image along the MEP was denoted as the transition state. The energy barrier E_a of each elementary reaction was calculated by the energy difference between the transition state and initial state. The corresponding reaction energy ΔE was calculated by the energy difference between the final state and initial state. By convention, positive values of E_b and ΔE indicate an endothermic process, while negative values an exothermic process.

3. RESULTS AND DISCUSSION

3.1. Geometry and Stability of M-BNNSs. The geometries and stability of several M-BNNSs are first investigated. We have considered two types of monovacancy from the defect-free h-BNNS: one is formed by removing a single boron
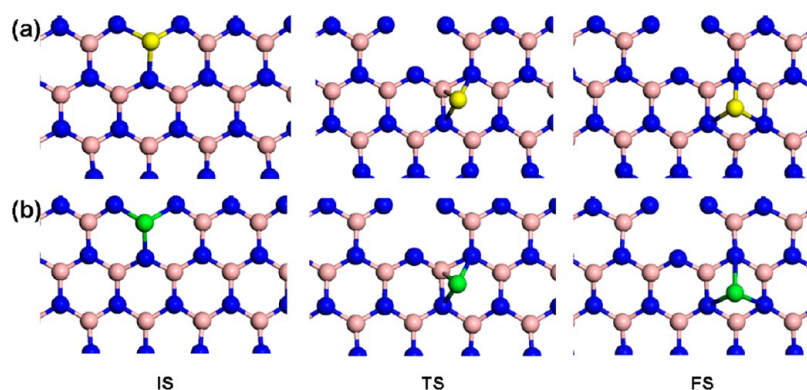
Figure 2. Geometries of the IS, TS, and FS (top view) for moving a single Co (a) or Fe (b) metal atom from the B-vacancy to the nearby hollow site. Color scheme: Co, yellow; Fe, green; B, pink; N, dark blue.
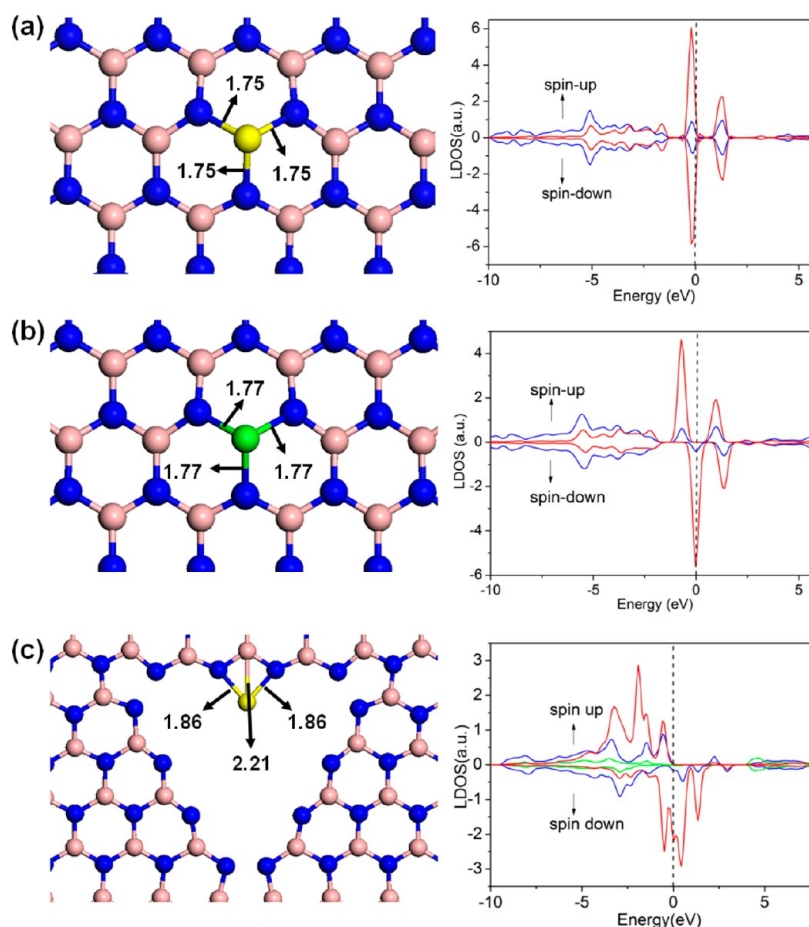

Figure 3. Left: the configurations of the h-BNNSs with the Co (a) or Fe (b) embedded in the B-vacancy and h-BNNS with Co (c) embedded in the N-edge. Right: the corresponding spin polarized LDOS projected on metal-3d (red), N-2p (blue), and B-2p (green) orbitals in the Co or Fe embedded h-BNNS with the B-vacancy and the Co embedded h-BNNS with the N-edge. The Fermi level was set to zero. Color scheme: Co, yellow; Fe, green; B, pink; N, dark blue; C, black; O, red.

atom, and the other is generated by removing a single nitrogen atom. Since B-vacancy is more stable than nitrogen vacancy as shown by both experiment and theory,[16,17] we focus here on M-BNNSs with metal atoms (Cu, Ag, Au, Pt, Rh, Pd, Fe, Co, and Ir) embedded in the B-vacancy. Nonetheless, the M-BNNS with a Co atom embedded in the N-edge defect is also explored, which is quite expensive computationally as it consists of 113 atoms in the unit cell.

In the case of the B-vacancy, the metal atom was found to lie at the center of the defect with three equivalent M−N bonds.

As shown in Table 1, the M−N bond lengths increase in the order Co < Fe < Cu < Ir = Rh < Pt = Pd < Au < Ag. The longest Ag−N bond is 2.12 Å while the shortest Co−N bond is 1.75 Å. In our previous study of the Ru-BNNS,[21] the bond length between the Ru atom and each nitrogen atom was calculated to be 1.91 Å, which is between these two limiting values. Because of the large sizes, these metal atoms are out of the h-BNNS plane. As listed in Table 1, the vertical displacement of the metal atoms out of the h-BNNS plane are calculated between 1.03 and 1.66 Å. On the other hand, the
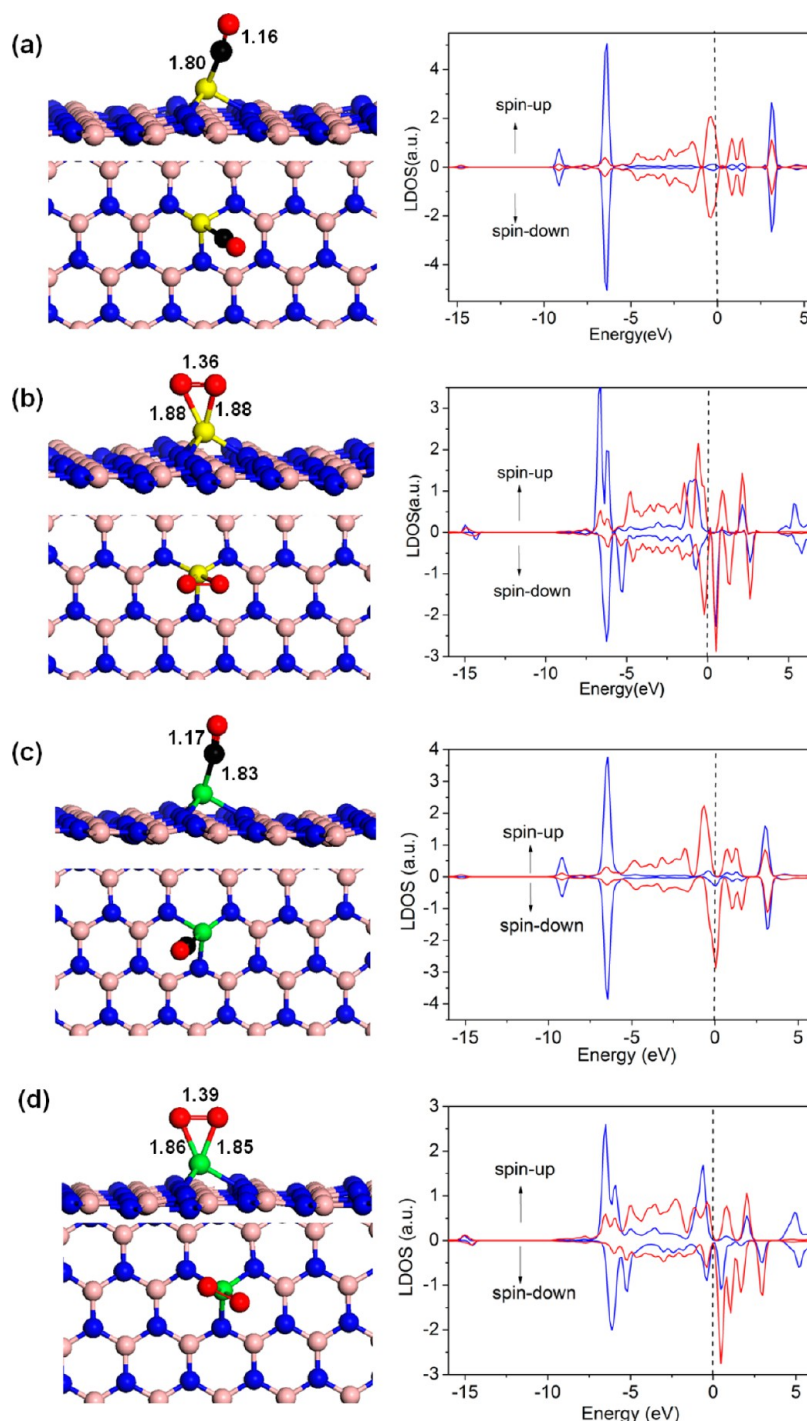
Figure 4. Left: side and top views of the most energetically favorable configurations of CO and O_2 adsorbed on the h-BNNSs with Co (a, b) and Fe (c, d) embedded in the B-vacancy. Right: the corresponding spin-polarized LDOS. Red and blue curves denote the d-projected LDOS of the metal and the p-projected LDOS of CO/O_2, respectively.

Co atom locates between two N atoms in the N-edge defect with the Co–N bond distances of 1.86 Å, slightly longer than that in the B-vacancy (1.75 Å). In this configuration, the Co atom is in the plane of the h-BNNS.

In order to evaluate the stability of the M-BNNS, which is essential for its applications at high temperatures, the binding energies of the metal atom at the B-vacancy was investigated. Similar to the Ru atom, the metal binding at the defect site on the h-BNNS is very strong for all metals studied here. As shown in Table 1, the binding strength decreases in the order Ir > Co

> Fe > Rh > Pt > Cu > Pd > Au > Ag with the binding energy of −9.21, −8.64, −8.54, −8.41, −6.53, −5.64, −5.24, −3.03, and −3.02 eV, respectively. These numbers can be compared with the binding energy of B at this site (−7.62 eV).[17] The interaction between a single metal atom and the defect-free h-BNNS is also explored in this work, and it is relatively weak with the adsorption energies of −0.14, 0.08, −0.03, −1.51, −1.03, −0.94, −0.52, −0.50, and −1.23 eV for Cu, Ag, Au, Pt, Rh, Pd, Fe, Co, and Ir atom, respectively. Since these values are significantly smaller than those at the defect site, it is clear that
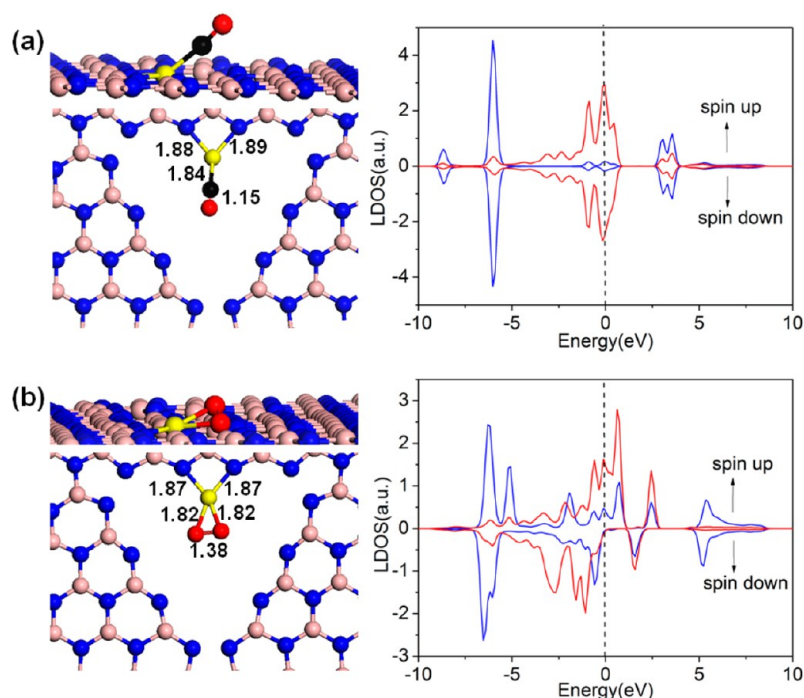
Figure 5. Left: side and top views of the most energetically favorable configurations of CO (a) and O_2 (b) adsorbed on the h-BNNS with Co embedded in the N-edge. Right: the corresponding spin-polarized LDOS. Red and blue curves denote the d-projected LDOS of the metal and the p-projected LDOS of CO/O_2, respectively.

the defect sites are vital in producing stable M-BNNS. To further understand the mobility of the metal atoms within the h-BNNS, we also investigated the barrier of the Co or Fe atom for moving out of the defect binding site to a neighboring hollow site. Figure 2 shows the structures of the initial state, transition state, and final state for this process, respectively. The calculated energy barriers (6.34 eV for Co and 6.39 eV for Fe) are very large, close to the value obtained on the Ru-BN sheet[21] and much higher than that on the copper embedded graphene (2.34 eV).[3] These results suggest that metal atoms bind strongly in the defects of h-BNNSs and M-BNNSs are likely to have comparable stabilities to defect-free h-BNNSs.

To explore the binding nature of the metal−BN interaction, we have performed Bader charge density analyses[34] for the most stable configuration of the M-BNNSs. As listed in Table 1, all metal atoms have positive charges, which are in the order of Au < Pt < Ag < Pd < Rh < Ir < Cu < Co < Fe. Clearly, there is significant electron transfer from the metal atom to the BN sheet, which is likely responsible for the stabilization of single metal atoms, and may even account for the catalytic activity of M-BNNSs catalysts, as discussed below.

To gain a deeper understanding of the interaction between the embedded metal atoms and defect sites of h-BNNSs, the spin-polarized local densities of states (LDOSs) projected onto the metal-3d and neighboring N-2p orbitals are computed. To reduce computational costs, we only examined the Co and Fe atoms embedded in h-BNNSs. From the LDOSs plotted in Figure 3a,b, the 3d orbitals of the Co or Fe atom are shown to strongly mix with the 2p orbitals of the N atoms above and below the Fermi level (E_F), suggesting a very strong interaction between the metal atom and B-vacancy. Similarly, in the case of the Co embedded h-BNNS with the N-edge defect, this hybridization was also found to be strong. On the other hand, the overlap between the 3d orbitals of Co and the 2p orbitals of the B atoms is quite small and can be ignored, consistent with

the long Co−B distances (2.21 Å). The strong metal−ligand interaction resembles more closely homogeneous catalysts than heterogeneous catalysts, particularly metal surfaces.

In general, the strong coupling between the 3d orbitals of the metal atom and 2p orbitals of the nitrogen atoms makes metal atoms very stable in M-BNNSs.[35] As shown below, these localized metal d orbitals near E_F also play a crucial role in activating the O_2 reactant in the CO oxidation reaction.

3.2. Adsorption of CO and O_2 on M-BNNSs. The oxidation of CO is a well understood, prototypical heterogeneous catalytic reaction.[21,23,36−39] For this reason, it is chosen in this work as a probe reaction to explore the catalytic activity of the M-BNNS. We first examine the adsorption of CO and O_2 on the M-BNNS. Both CO and O_2 are found to strongly interact with the M-BNNS at the metal site, and the calculated binding energies are summarized in Table 1.

For CO, it adsorbs with its carbon end at the metal site with a tilted angle. The adsorption pattern is very similar to those on metal-embedded graphene[2,3,5] and boron nitride nanotubes.[40] As shown in Table 1, the order for the calculated binding energies is Ir > Pt > Au > Rh > Fe > Pd > Co > Ag > Cu. For Ir-BNNS, which has the strongest adsorption, the binding energy is calculated to be −2.29 eV, which is about 1.45 eV stronger than that of Cu-BNNS, which shows the weakest adsorption. The CO bond length changes slightly between 1.15 and 1.17 Å, indicating minimal perturbation of its electronic structure by adsorbing on M-BNNS. For example, as shown in Figure 4a, on Co-BNNS, the C−O bond length (1.16 Å) is about 0.02 Å longer than that of an isolated CO molecule and the C−Co bond length is found to be 1.80 Å. For Fe-BNNS (see Figure 4c), the C−O bond length also changes only a little and the distance of C−Fe is about 1.83 Å, close to those on Co-BNNS.

For the O_2 molecule, the preferred adsorption pattern is nearly parallel to the M-BNNS with two M−O bonds formed,

17323

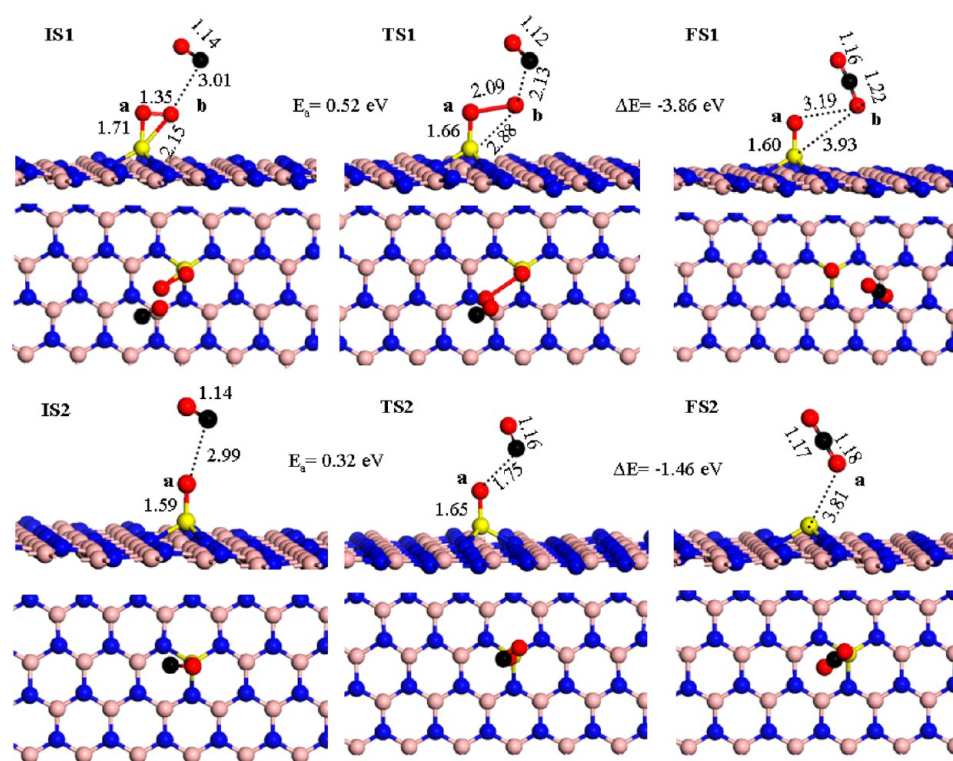dx.doi.org/10.1021/jp4055445 | J. Phys. Chem. C 2013, 117, 17319−17326

Figure 6. Geometries (side and top views) of initial state (IS), transition state (TS), and final state (FS) for both steps in ER CO oxidation on the h-BNNS with Co embedded in the B-vacancy.

rather different from CO. The adsorption is quite strong, and the order for the binding energy is changed to Ir > Fe > Pt > Pd > Rh > Co > Au > Ag > Cu. The strongest one is -2.37 eV on Ir-BNNS, and the weakest one is -0.54 eV on Cu-BNNS. Interestingly, the O_2 bond length in its adsorbed state is significantly elongated from that (1.23 Å) in the gas phase molecule. As listed in Table 1, the shortest O−O bond length is on Ag-BNNS and the longest is on Ir-BNNS with values of 1.31 and 1.43 Å, respectively. As displayed in Figure 4b,d, the calculated O−O bond length on Co-BNNS and Fe-BNNS increases to 1.36 and 1.39 Å, respectively. In the case of Co-BNNS with the N-edge, O_2 also adsorbs with a parallel configuration and the O−O distance has a similar value of 1.38 Å. The elongation of the O−O bond suggests that the adsorbed oxygen molecule is activated by the metal center.

The calculated binding energies indicate that there might be a competition between the CO and O_2 adsorption at the metal site. When O_2 binds stronger than CO, the metal center will be likely covered with the O_2 species. Conversely, the metal site will be overpopulated by CO if it binds stronger than O_2, which might poison the catalyst. Based on our calculations, O_2 is expected to preferentially occupy the Fe, Co, Ir, and Pd atom sites allowing reaction with the incoming gas phase CO species via an Eley−Rideal (ER) type mechanism. However, for Cu, Ag, Au, Pt, and Rh atom sites, CO adsorption dominates, and as the ER mechanism is not possible. In such cases, these catalysts would be rapidly poisoned under reaction conditions.

To gain more insight into how CO and O_2 interact with M-BNNSs, the electronic structures of these two species adsorbed on Co-BNNSs and Fe-BNNSs with the metal embedded at the B-vacancy are analyzed. As evidenced by the LDOSs in Figure 4a,c, the mixing between the 3d orbitals of Co or Fe and CO-2p orbitals is weak near E_F, which is very similar to the case on the Fe-embedded graphene oxide surface.[5] The lack of strong

mixing between these orbitals is consistent with the small change in the C−O bond length and the relatively weak adsorption for CO at the metal site. However, as shown in the LDOS plot, there are still some small couplings between the d orbitals of Co or Fe and orbitals of CO below and above E_F. It is noted that CO can donate its two electrons via σ-donation to the metal 3d orbital of the transition metals (the coupling around and below E_F). On the other hand, CO can also serves as a strong π-acceptor possessing of an antibonding $2\pi^*$ molecular orbital (the farthest coupling above E_F).[41] Similar observations have been made for Co-BNNS with the N-edge.

As discussed above, the elongation of the O−O bond in adsorbed O_2 molecule implies strong interaction with the metal center. The LDOS for the M-3d and O-2p orbitals is also displayed in Figure 4b,d. In comparison with the CO adsorption, a much stronger mixing between the metal 3d orbitals and O_2 2p orbitals near E_F can be clearly seen, which is almost certainly responsible for the significant weakening of the O−O bond length and strong adsorption of O_2. Quantifying this activation of molecular oxygen, a Bader charge analysis reveals a $0.27e$ and $0.33e$ charge transfer from the Co- and Fe-BNNS, respectively, into the $2\pi^*$ antibonding orbital of O_2, consistent with the O−O bond length elongation observed.

From the above discussion, it is concluded that O_2 is strongly activated by the metal center in M-BNNSs while CO is not. Accordingly, it is likely that CO oxidation will proceed with CO pulling one oxygen atom from the adsorbed O_2 though the ER mechanism. If CO has a much stronger adsorption energy than that of O_2, it might block the metal sites for O_2 adsorption, thus precluding the opportunity for oxygen to be activated.[38]

It can be seen from Table 1 that, for the Fe, Co, Ir, and Pd embedded h-BNNSs, the O_2 adsorption is stronger than CO. Given the fact that the earth-abundant Co and Fe are much cheaper than Ir and Pd, Co-BNNSs or Fe-BNNSs are more

promising candidates for low-cost, high-activity, and thermally stable catalysts.

3.3. CO Oxidation. In this work, only the ER mechanism is considered for CO oxidation as a probe of the catalytic activity of M-BNNSs. To this end, the Co-BNNS was selected as the example. The first ER reaction step proceeds as follows: Co-BNNS + O_2(gas) + CO(gas) → Co-BNNS-O_2(ads) + CO(gas) → Co-BNNS-O(ads) + CO_2(ads) → Co-BNNS-O(ads) + CO_2(gas). We note in passing that CO can also be oxidized by following the Langmuir−Hinshelwood mechanism, which requires both CO and O_2 adsorbed. However, this mechanism is not investigated here.

The configurations for the initial state (IS), transition state (TS), and final state (FS) along the reaction path are displayed in Figure 6, where the primary bond lengths are also given. The kinetic and thermodynamic information about the reaction is listed in Table 2. In IS1, O_2 was found to adsorb at the Co site

Table 2. Calculated Activation and Reaction Energies (eV) for the Reactions of CO + O_2 → CO_2 + O and CO + O → CO_2[a]

reaction	type	E_a	ΔE
CO + O_2 → CO_2 + O	ER mechanism	0.52	−3.86
CO + O → CO_2	ER mechanism	0.32	−1.46

[a]The corresponding structures for IS, TS and FS are displayed in Figure 6.

with the O_a−O_b bond length elongated from 1.23 Å in the isolated O_2 molecule to 1.35 Å, while CO is located above the M-BNNS. The distance between the C atom and the O_b atom of O_2 was calculated to be 3.01 Å. At TS1, the O_a−O_b bond length was about 2.09 Å, and the distance of C−O_b became much shorter with a value of 2.13 Å. After reaction, the CO_2 molecule (FS1) was formed with one atomic oxygen atom (O_a) adsorbed atop of Co. As shown in Table 2, this exothermic reaction (ΔE = −3.86 eV) has a barrier of 0.52 eV.

We have also investigated whether a second ER step, in which CO is oxidized by the remaining O_a after the first step, is possible after the generation of the first CO_2 product. As showed in Figure 6, a parallel configuration of the CO molecule more than 1.75 Å away from the O_a atom preadsorbed on Co is chosen as the initial state (IS2). At TS2, the carbon atom of CO attacks the O_a atom with the C−O_a distance of 2.99 Å. At FS2, a CO_2 molecule is produced above the metal site with the distance of Co−O_a to be 3.01 Å. The barrier for this step is calculated to be 0.32 eV, and the exothermicity is −1.46 eV. After CO_2 desorption, the Co-BNNS catalyst is recovered for a new cycle of CO oxidation.

The barriers for both ER steps are slightly lower than those on Fe or Cu embedded graphene catalysts (0.58 and 0.54 eV)[3,4] and much lower than those of conventional noble metal based catalysts (~1.0 eV).[23,42,43] Such a high activity of the Co-embedded h-BNNS may be attributed to the resonance among the 3d orbitals of the Co atom and 2p orbitals of O_2. The low barriers suggest that the catalysis of CO oxidation may be viable on M-BNNSs at much lower temperatures than that on conventional catalysts. Also, the superb thermal stability of the M-BNNSs also allows them to be employed at high temperatures. M-BNNSs have added advantage as catalysts because of their high surface area and abundant active metal centers.

4. CONCLUSIONS

In this work, the hexagonal boron nitride nanosheets with metal (M = Cu, Ag, Au, Pt, Rh, Pd, Fe, Co, and Ir) embedded in various defect sites (M-BNNSs) were investigated by using a DFT method. From the calculations, the single metal atom embedded h-BNNSs are shown to have comparable stabilities to defect-free h-BNNSs. To explore the catalytic capacity of M-BNNSs, CO oxidation was studied on the Co-BNNS. Although both CO and O_2 adsorb at the metal site, only the latter is activated. The activation is attributed to the strong mixing between the metal 3d orbitals and the 2p orbitals of O_2, based on the LDOS analysis. Finally, the CO oxidation barriers in the Eley−Rideal pathway were calculated for both molecular and atomic oxygens adsorbed on the metal site. The calculated barriers are much lower than those found on metal surfaces, suggesting that the catalytic CO oxidation by the Co-BNNS might be viable at low temperatures. Given the high surface area and high thermal stability, our results reported here suggest that M-BNNSs might be a good candidate for low-cost, highly active, and stable catalysts for oxidation reactions.

■ AUTHOR INFORMATION

Corresponding Author

*Phone +86-591-83969175; e-mail slin@fzu.edu.cn (S.L.).

Notes

The authors declare no competing financial interest.

■ REFERENCES

(1) Yoo, E.; Okata, T.; Akita, T.; Kohyama, M.; Nakamura, J.; Honma, I. Enhanced Electrocatalytic Activity of Pt Subnanoclusters on Graphene Nanosheet Surface. *Nano Lett.* **2009**, 9, 2255−2259.

(2) Lu, Y. H.; Zhou, M.; Zhang, C.; Feng, Y. P. Metal-Embedded Graphene: A Possible Catalyst with High Activity. *J. Phys. Chem. C* **2009**, 113, 20156−20160.

(3) Song, E. H.; Wen, Z.; Jiang, Q. CO Catalytic Oxidation on Copper-Embedded Graphene. *J. Phys. Chem. C* **2011**, 115, 3678−3683.

(4) Li, Y. F.; Zhou, Z.; Yu, G. T.; Chen, W.; Chen, Z. F. CO Catalytic Oxidation on Iron-Embedded Graphene: Computational Quest for Low-Cost Nanocatalysts. *J. Phys. Chem. C* **2010**, 114, 6250−6254.

(5) Li, F. Y.; Zhao, J. J.; Chen, Z. F. Fe-Anchored Graphene Oxide: A Low-Cost and Easily Accessible Catalyst for Low-Temperature CO Oxidation. *J. Phys. Chem. C* **2011**, 116, 2507−2514.

(6) Dean, C. R.; Young, A. F.; Meric, I.; Lee, C.; Wang, L.; Sorgenfrei, S.; Watanabe, K.; Taniguchi, T.; Kim, P.; Shepard, K. L.; et al. Boron Nitride Substrates for High-Quality Graphene Electronics. *Nat. Nanotechnol.* **2010**, 5, 722−726.

(7) Watanabe, K.; Taniguchi, T.; Kanda, H. Direct-Bandgap Properties and Evidence for Ultraviolet Lasing of Hexagonal Boron Nitride Single Crystal. *Nat. Mater.* **2004**, 3, 404−409.

(8) Zhi, C. Y.; Bando, Y.; Tang, C. C.; Kuwahara, H.; Golberg, D. Large-Scale Fabrication of Boron Nitride Nanosheets and Their Utilization in Polymeric Composites with Improved Thermal and Mechanical Properties. *Adv. Mater.* **2009**, 21, 2889−2893.

(9) Wu, J. C. S.; Chen, W. C. A Novel BN Supported Bi-Metal Catalyst for Selective Hydrogenation of Crotonaldehyde. *Appl. Catal., A* **2005**, *289*, 179−185.

(10) Kim, G.; Jang, A. R.; Jeong, H. Y.; Lee, Z.; Kang, D. J.; Shin, H. S. Growth of High-Crystalline, Single-Layer Hexagonal Boron Nitride on Recyclable Platinum Foil. *Nano Lett.* **2013**, *13*, 1834−1839.

(11) Golberg, D.; Bando, Y.; Huang, Y.; Terao, T.; Mitome, M.; Tang, C.; Zhi, C. Boron Nitride Nanotubes and Nanosheets. *ACS Nano* **2010**, *4*, 2979−2993.

(12) Tang, S. B.; Cao, Z. X. Structural and Electronic Properties of the Fully Hydrogenated Boron Nitride Sheets and Nanoribbons: Insight from First-Principles Calculations. *Chem. Phys. Lett.* **2010**, *488*, 67−72.

(13) Yazyev, O. V.; Pasquarello, A. K. Metal adatoms on graphene and hexagonal boron nitride: Towards Rational Design of Self-Assembly Templates. *Phys. Rev. B* **2008**, *82*, 045407.

(14) Grad, G. B.; Blaha, P.; Schwarz, K.; Auwarter, W.; Greber, T. Density Functional Theory Investigation of the Geometric and Spintronic Structure of h-BN/Ni(111) in View of Photoemission and Stm Experiments. *Phys. Rev. B* **2003**, *68*, 085404.

(15) Lin, Y.; Bunker, C. E.; Fernando, K. A.; Connell, J. W. Aqueously Dispersed Silver Nanoparticle-Decorated Boron Nitride Nanosheets for Reusable, Thermal Oxidation-Resistant Surface Enhanced Raman Spectroscopy (Sers) Devices. *ACS Appl. Mater. Interfaces* **2012**, *4*, 1110−1117.

(16) Jin, C. H.; Lin, F.; Suenaga, K.; Iijima, S. Fabrication of a Freestanding Boron Nitride Single Layer and Its Defect Assignments. *Phys. Rev. Lett.* **2009**, *102*, 195505.

(17) Du, A. J.; Chen, Y.; Zhu, Z. H.; Amal, R.; Lu, G. Q.; Smith, S. C. Dots Versus Antidots: Computational Exploration of Structure, Magnetism, and Half-Metallicity in Boron−Nitride Nanostructures. *J. Am. Chem. Soc.* **2009**, *131*, 17354−17359.

(18) Gao, M.; Lyalin, A.; Taketsugu, T. CO Oxidation on h-BN Supported Au Atom. *J. Chem. Phys.* **2013**, *138*, 034701.

(19) Gao, M.; Lyalin, A.; Taketsugu, T. Catalytic Activity of Au and Au_2 on the h-BN Surface: Adsorption and Activation of O_2. *J. Phys. Chem. C* **2012**, *116*, 9054−9062.

(20) Gao, M.; Lyalin, A.; Taketsugu, T. Oxygen Activation and Dissociation on h-BN Supported Au Atoms. *Int. J. Quantum Chem.* **2013**, *113*, 443−452.

(21) Huang, C. J.; Ye, X. X.; Chen, C.; Lin, S.; Xie, D. Q. A Computational Investigation of CO Oxidation on Ruthenium-Embedded Hexagonal Boron Nitride Nanosheet. *Comput. Theor. Chem.* **2013**, *1011*, 5−10.

(22) Joo, S. H.; Park, J. Y.; Renzas, J. R.; Butcher, D. R.; Huang, W. Y.; Somorjai, G. A. Size Effect of Ruthenium Nanoparticles in Catalytic Carbon Monoxide Oxidation. *Nano Lett.* **2010**, *10*, 2709−2713.

(23) Royer, S.; Duprez, D. Catalytic Oxidation of Carbon Monoxide over Transition Metal Oxides. *ChemCatChem* **2011**, *3*, 24−65.

(24) Kresse, G.; Hafner, J. Ab Initio Molecular Dynamics for Liquid Metals. *Phys. Rev. B* **1993**, *47*, 558−561.

(25) Kresse, G.; Furthmüller, J. Efficient Iterative Schemes for Ab Initio Total-Energy Calculations Using a Plane-Wave Basis Set. *Phys. Rev. B* **1996**, *54*, 11169−11186.

(26) Kresse, G.; Furthmüller, J. Efficiency of Ab-Initio Total Energy Calculations for Metals and Semiconductors Using a Plane-Wave Basis Set. *Comput. Mater. Sci.* **1996**, *6*, 15−50.

(27) Perdew, J. P.; Chevary, J. A.; Vosko, S. H.; Jackson, K. A.; Pederson, M. R.; Singh, D. J.; Fiolhais, C. Atoms, Molecules, Solids, and Surfaces: Applications of the Generalized Gradient Approximation for Exchange and Correlation. *Phys. Rev. B* **1992**, *46*, 6671−6687.

(28) Blöchl, P. E. Projector Augmented-Wave Method. *Phys. Rev. B* **1994**, *50*, 17953−17979.

(29) Kresse, G.; Joubert, D. From Ultrasoft Pseudopotentials to the Projector Augmented-Wave Method. *Phys. Rev. B* **1999**, *59*, 1758−1775.

(30) Paszkowicz, W.; Pelka, J. B.; Knapp, M.; Szyszko, T.; Podsiadlo, S. Lattice Parameters and Anisotropic Thermal Expansion of Hexagonal Boron Nitride in the 10−297.5 K Temperature Range. *Appl. Phys. A: Mater. Sci. Process.* **2002**, *75*, 431−435.

(31) Sen, D.; Thapa, R.; Bhattacharjee, K.; Chattopadhyay, K. K. Site Dependent Metal Adsorption on (3×3) h-BN Monolayer: Stability, Magnetic and Optical Properties. *Comput. Mater. Sci.* **2012**, *51*, 165−171.

(32) Monkhorst, H. J.; Pack, J. D. Special Points for Brillouin-Zone Integrations. *Phys. Rev. B* **1976**, *13*, 5188−5192.

(33) Henkelman, G.; Uberuaga, B. P.; Jonsson, H. A Climbing Image Nudged Elastic Band Method for Finding Saddle Points and Minimum Energy Paths. *J. Chem. Phys.* **2000**, *113*, 9901−9904.

(34) Henkelman, G.; Arnaldsson, A.; Jonsson, H. A Fast and Robust Algorithm for Bader Decomposition of Charge Density. *Comput. Mater. Sci.* **2006**, *36*, 254−360.

(35) Stamenkovic, V.; Mun, B. S.; Mayrhofer, K. J.; Ross, P. N.; Markovic, N.; Rossmeisl, J.; Greeley, J.; Nørskov, J. K. Changing the Activity of Electrocatalysts for Oxygen Reduction by Tuning the Surface Electronic Structure. *Angew. Chem., Int. Ed.* **2006**, *45*, 2897−2901.

(36) Qiao, B. T.; Wang, A. Q.; Yang, X. F.; Allard, L. F.; Jiang, Z.; Cui, Y. T.; Liu, J. Y.; Li, J.; Zhang, T. Single-Atom Catalysis of CO Oxidation Using Pt_1/FeO_x. *Nat. Chem.* **2011**, *3*, 634−641.

(37) Chen, M. S.; Cai, Y.; Yan, Z.; Gath, K. K.; Axnanda, S.; Goodman, D. W. Highly Active Surfaces for CO Oxidation on Rh, Pd, and Pt. *Surf. Sci.* **2007**, *601*, 5326−5331.

(38) Fu, Q.; Li, W. X.; Yao, Y. X.; Liu, H. Y.; Su, H. Y.; Ma, D.; Gu, X. G.; Chen, L. M.; Wang, Z.; Zhang, H.; et al. Interface-Confined Ferrous Centers for Catalytic Oxidation. *Science* **2010**, *328*, 1141−1144.

(39) Johnson, R. S.; DeLaRiva, A.; Ashbacher, V.; Halevi, B.; Villanueva, C. J.; Smith, G. K.; Lin, S.; Datye, A. K.; Guo, H. The CO Oxidation Mechanism and Reactivity on PdZn Alloys. *Phys. Chem. Chem. Phys.* **2013**, *15*, 7768−7776.

(40) Xie, Y.; Huo, Y. P.; Zhang, J. M. First-Principles Study of CO and NO Adsorption on Transition Metals Doped (8,0) Boron Nitride Nanotube. *Appl. Surf. Sci.* **2012**, *258*, 6391−6397.

(41) Wannakao, S.; Nongnual, T.; Khongpracha, P.; Maihom, T.; Limtrakul, J. Reaction Mechanisms for CO Catalytic Oxidation by N_2O on Fe-Embedded Graphene. *J. Phys. Chem. C* **2012**, *116*, 16992−16998.

(42) Lopez, N.; Janssens, T. V. W.; Clausen, B. S.; Xu, Y.; Mavrikakis, M.; Bligaard, T.; Nørskov, J. K. On the Origin of the Catalytic Activity of Gold Nanoparticles for Low-Temperature CO Oxidation. *J. Catal.* **2004**, *223*, 232−235.

(43) Su, H. Y.; Yang, M. M.; Bao, X. H.; Li, W. X. The Effect of Water on the CO Oxidation on Ag(111) and Au(111) Surfaces: A First-Principle Study. *J. Phys. Chem. C* **2008**, *112*, 17303−17310.